mater.scichina.com link.springer.com

Published online 9 November 2023 | https://doi.org/10.1007/s40843-023-2599-9
Sci China Mater 2023, 66(12): 4680–4688

CdS/COF core-shell nanorods with efficient chemisorption, enhanced carrier separation, and antiphotocorrosion ability for U(VI) photoreduction

Kaifu Yu[1†], Pan He[1†], Ningning He[1], Xiaofeng Li[1], Changxue Dong[2], Bo Jiang[1], Yingdi Zou[1], Xiang Pei[1], Yang Li[1*] and Lijian Ma[1*]

ABSTRACT **Reduction of soluble U(VI) to insoluble U(IV) based on semiconductor photocatalysts is a favored U(VI)-extraction method, because of its simplicity, environmental friendliness, and high efficiency. The key to implement this technology is the development of efficient photocatalysts with high activity and stability for sacrificial agents-free U(VI) photoreduction. Herein, we report a new type of CdS/covalent organic framework (COF) core-shell photocatalysts (CdS@COF-*X*, *X* = 5, 10, 15, and 20) with efficient chemisorption, enhanced carrier separation, and antiphotocorrosion ability for U(VI) photoreduction without additional sacrificial agents. The two-dimensional COF, formed by the polycondensation of 2,4,6-triformylphloroglucinol and 1,3,5-tris(4-aminophenyl)triazine, was selected to construct the hybrid materials due to its high chemical stability, matching band gaps and efficient chemisorption for U(VI). Remarkably, CdS@COF-10 realized a record high U(VI) extraction capacity of 1825.6 mg g^{-1} after 90 min. Moreover, the reduction ratio of uranium was up to 82.5%, and the product was identified as uranium dioxide (UO_2) after reaction. Further mechanistic studies indicated that the COF shell not only provided chemisorption sites for U(VI) to decrease the activation energy of U(VI) reduction, but also formed a strong built-in electric field at the interface with the CdS core to promote the carrier separation. More importantly, for all CdS@COF-*X*, CdS-COF-10 with appropriate COF shell content balanced the crystallinity, interfacial contact integrity, light absorption of CdS core, and number of U(VI) chemisorption sites, achieving the highest carrier separation efficiency and U(VI) photoreduction performance.**

Keywords: covalent organic frameworks, core-shell structures, U(VI) photoreduction, carrier separation, antiphotocorrosion

INTRODUCTION

Efficient uranium extraction from nuclear wastewater is a crucial environmental concern owing to the high chemical toxicity and radioactivity of uranium [1–3]. The solubility of uranium oxidation states widely varies, making it effective to extract uranium by reducing soluble U(VI) to insoluble U(IV) [4–6]. Among the available reduction methods, U(VI) photoreduction is a favored reduction method because of its simplicity, environmental friendliness, and high efficiency, where the key to implement this technology is the development of advanced photocatalysts [7,8]. Up to now, various semiconductor materials have been explored for U(VI) photoreduction, including transition metal sulfides, transition metal oxides, and organic semiconductors [9–16]. Among them, transition metal sulfides are particularly promising, due to their low cost, strong light absorption, and ability to realize U(VI) photoreduction without additional sacrificial agents [17–20]. For instance, the complex SnO_2/$CdCO_3$/CdS nanocomposite attained a U(VI) extraction efficiency of 80% after 70 min towards sacrificial agents-free U(VI) photoreduction [17]. Recently, Dong *et al.* [18] developed the Te-doped CdS nanobelts for U(VI) photoreduction, realizing a U(VI) extraction efficiency of 97.4% and a U(VI) extraction capacity of 836 mg g^{-1} after 140 min without any sacrificial agents. However, the reported transition metal sulfides generally suffer from severe deficiency of U(VI) chemisorption sites, photogenerated carrier recombination, and photocorrosion issues, leading to catalyst damage and activity decline [7]. Therefore, developing photocatalysts with excellent activity and stability for sacrificial agents-free U(VI) photoreduction is an urgent requirement, but undoubtedly remains a grand challenge.

Designing heterojunction for carrier transfer through the interface is a traditional but effective approach for carrier separation [21,22]. In particular, constructing a core-shell structure can maximize the contact effect and reduce the carrier transport distance, further optimizing the carrier separation efficiency [23,24]. Additionally, the shell materials in the core-shell structure can effectively constrain the core materials, providing the antiphotocorrosion ability [25,26]. More importantly, selecting shell materials with U(VI) chemisorption sites is able to compensate for the lack of these sites in core materials and promote photocatalytic performance.

As a new type of porous materials, covalent organic frameworks (COFs) have garnered extensive attention for their applications in adsorption, catalysis, energy storage, and so on [27–29]. Due to their fast carrier transfer and strong visible absorption performance, COFs are ideal shell materials for combining with semiconductors [30,31]. Furthermore, thanks to their adjustable ordered pores and active sites and the composition of the different structural units and functional groups, COFs are also excellent adsorbents for U(VI) extraction [32–34]. In fact, various covalently linked COFs have been used for U(VI)

[1] College of Chemistry, Key Laboratory of Radiation Physics & Technology, Ministry of Education, Sichuan University, Chengdu 610064, China
[2] College of Materials Science and Engineering, Sichuan University, Chengdu 610064, China
[†] These authors contributed equally to this work.
[*] Corresponding authors (emails: ly7701850@163.com (Li Y); ma.lj@hotmail.com (Ma L))

photoreduction, including imine, hydrazone, and β-ketoenamine [35,36]. Among them, the β-ketoenamine COFs were synthesized by the combination of reversible imine polycondensation and irreversible proton tautomerism (from enol structure to keto structure), possessing the advantages such as easy synthesis, high stability, and large specific surface area, and thus have attracted much attention [37]. For example, Hu's research group [38] constructed the β-ketoenamine COF containing triazine unit (TpTt), which showed good U(VI) adsorption and photoreduction properties, achieving the U(VI) removal ratio of 76%. Recently, Hu's research group [39] further synthesized a series of isostructural β-ketoenamine COFs with different functional groups for U(VI) photoreduction. Although methanol was used as a sacrificial agent to capture holes in these studies, it is undeniable that β-ketoenamine COFs exhibit excellent potential for U(VI) photoreduction. Thus, utilizing transition metal sulfides as core materials and β-ketoenamine COFs as shell materials to construct novel catalysts with core-shell structures is a potential pathway to achieve high activity and stability towards U(VI) photoreduction.

Herein, we combined the advantages of CdS and COFs to elaborately design a new type of CdS/COF core-shell photocatalysts with high activity and stability for sacrificial agents-free U(VI) photoreduction. The two-dimensional (2D) β-ketoenamine COF, formed by the polycondensation of 2,4,6-triformylphloroglucinol (TFP) and 1,3,5-tris(4-aminophenyl)-triazine (TAPT), was selected to construct the hybrid materials due to its high chemical stability, matching band gaps and efficient chemisorption for U(VI) [40]. Furthermore, a series of CdS/COF core-shell nanorods with different amounts of COF shell (CdS@COF-*X*, *X* = 5, 10, 15, and 20) were synthesized through *in-situ* growing COF shell around CdS nanorods. Remarkably, CdS@COF-10 realized the fast extraction of U(VI), with the extraction rate constant of 0.092 min^{-1} and removal ratio of 98.8% after 90 min in a U(VI) solution with an initial concentration of 1 mmol L^{-1}. Moreover, the U(VI) extraction capacity *via* CdS@COF-10 reached up to 1825.6 mg g^{-1} after 90 min when the solid-to-liquid ratio was 0.1 g L^{-1}. In addition, CdS@COF-10 displayed outstanding stability during U(VI) photoreduction because of the excellent antiphotocorrosion ability derived from the protection of the COF shell. Further mechanistic studies indicated that COF shell not only provided chemisorption sites for U(VI) to decrease the activation energy of U(VI) reduction, but also formed a strong built-in electric field at the interface with CdS core to promote the carrier separation. More importantly, for all CdS@COF-*X*, CdS-COF-10 with appropriate COF shell content balanced crystallinity, interfacial contact integrity, light absorption of CdS core, and number of U(VI) chemisorption sites, achieving the highest carrier separation efficiency and U(VI) photoreduction performance.

EXPERIMENTAL SECTION

Preparation of P-CdS

Firstly, 228 mg of $CdCl_2{\cdot}2.5H_2O$ was dissolved in a mixture of 30 mL of ethylenediamine and 1 mL of deionized water with vigorous stirring. Next, 32 mg of sulfur powder and 3 mL of $N_2H_4{\cdot}H_2O$ were added sequentially to the resulting solution. After stirring for 30 min, the mixture was then heated to react at 120°C for 8 h. The resulting product was collected by centrifugation, washed thoroughly with water and ethanol on three separate occasions, and subsequently dried under vacuum to obtain the pure CdS (P-CdS).

Preparation of P-COF

The pure COF (P-COF) was prepared through a typical process. TFP (200 μmol) and TAPT (200 μmol) were added into a pressure tube, along with 2 mL of dioxane, 2 mL of *n*-butanol, and 0.5 mL of glacial acetic acid (AC). The mixture was subjected to ultrasound for 10 min and reacted at 120°C for 24 h. After that, the product was collected by suction filtration, and washed successively with dimethyl formamide (DMF) and methanol. The resulting powder was dried under vacuum to obtain P-COF.

Preparation of CdS@COF-*X*

Firstly, 20 mg of CdS and 400 mg of polyvinyl pyrrolidone (PVP) were dispersed in 10 mL of ethanol and stirred vigorously for 12 h. The resulting mixture was washed with ethanol and *n*-butanol, and then dispersed in 2 mL of *n*-butanol in a pressure tube to form a suspension. Next, TFP (*X* μmol) and TAPT (*X* μmol) were added into the pressure tube, along with 2 mL of dioxane. After ultrasound for 10 min, 0.1 mL of glacial AC was added to the pressure tube, which was then filled with nitrogen and reacted at 120°C for 24 h. CdS@COF-*X* (*X* = 5, 10, 15, and 20) was obtained by collecting the resulting product through suction filtration, followed by sequential washing with DMF and methanol. The product was then dried under vacuum to ensure complete dryness.

RESULTS AND DISCUSSION

Synthesis and structural characterizations

As illustrated in Fig. 1, P-COF was synthesized by the polycondensation of TFP and TAPT under solvothermal conditions using AC as catalyst. Besides, P-CdS was obtained by reducing a mixture of $CdCl_2{\cdot}2.5H_2O$ and sulfur powder by $N_2H_4{\cdot}H_2O$ under solvothermal conditions. Furthermore, P-CdS was dispersed in the *n*-butanol and dioxane mixed solution containing TFP, TAPT, and AC. Then, the resulting suspension was heated at 120°C for *in-situ* growing COF shell to obtain CdS@COF-*X* (*X* = 5, 10, 15, and 20) with different composition ratios of the shell and core. The ^{13}C solid-state nuclear magnetic resonance (NMR) spectrum was demonstrated that P-COF formed a more stable keto structure than enol structure through tautomerism (Fig. S1) [40,41]. Fig. 2a displays the transmission electron microscopy (TEM) image of P-CdS, where the lattice fringes of nanorods were clearly visible. As for the TEM images of CdS@COF-10 (Fig. 2b) and CdS@COF-20 (Fig. 2c), the morphologies of nanorods were well maintained and completely covered by COF shells. Furthermore, the COF shell thickness of CdS@COF-10 was just ~3.5 nm, while CdS@COF-20 possessed a COF shell thickness of over 10 nm. The high-angle-annular-dark-field scanning TEM (HAADF-STEM) image shows multiple crossover CdS@COF-10 nanorods (Fig. 2d). As indicated by the associated energy dispersive X-ray (EDX) elemental mapping images of CdS@COF-10, a uniform coating of the COF shell around the CdS core was evident as Cd, S, C, N, and O elements exhibited coincident distribution. As for CdS@COF-20 (Fig. S2), the distinct discrepancy in the distribution of Cd and S elements as compared with that of C, N, and O elements and even the

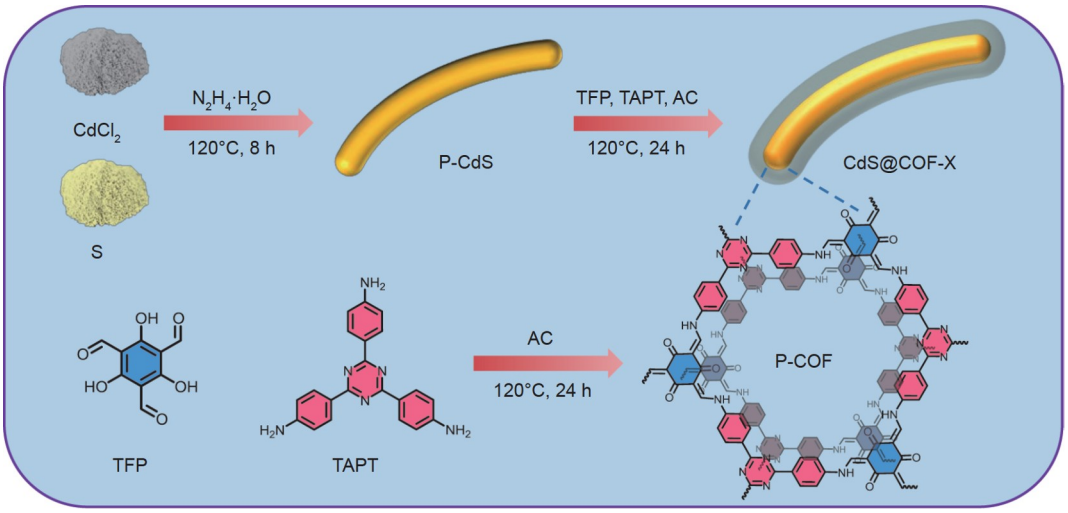

Figure 1 Schematic illustration for the synthesized process of CdS@COF-*X*.

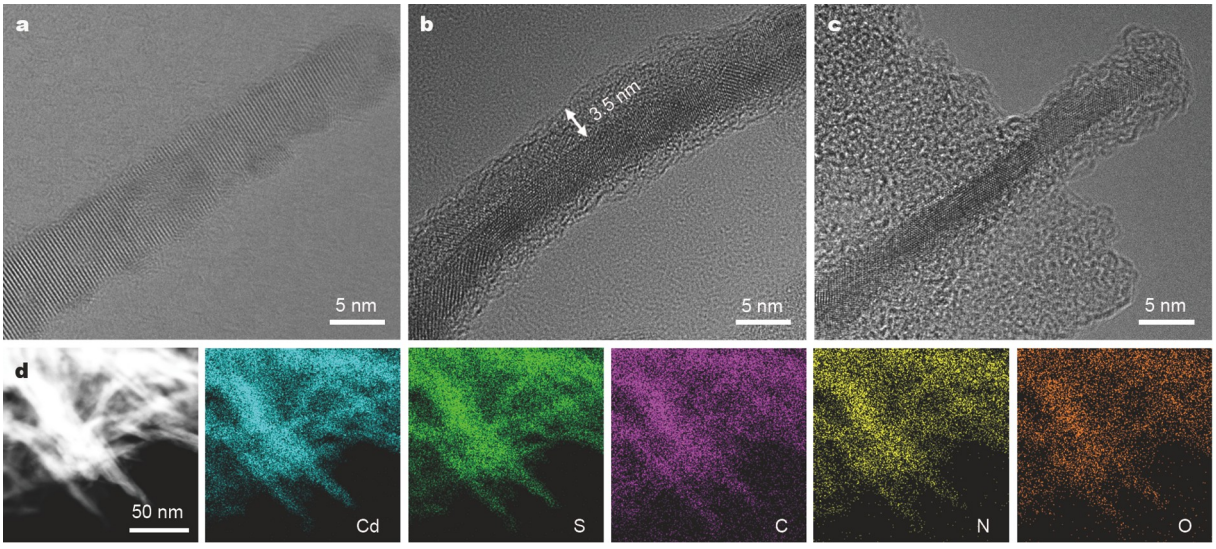

Figure 2 TEM images of (a) P-CdS, (b) CdS@COF-10, and (c) CdS@COF-20. (d) HAADF-STEM and the corresponding EDX elemental mapping images of CdS@COF-10.

presence of COF without CdS core were observed.

The crystal structures of P-COF, CdS@COF-*X* and P-CdS were further investigated by powder X-ray diffraction (PXRD). As shown in Fig. 3a, the structure of P-COF was ascribed to the AA stacking model, where the diffraction peaks at ~5.6°, ~9.7°, ~14.8°, and ~26.1° were assigned to the (100), (110), (120), and (001) facet, respectively. Furthermore, all the diffraction peaks in the PXRD pattern of P-CdS are consistent with the greenockite CdS phase (PDF#41-1049) (Fig. S3). As for the CdS@COF-*X* hybrid materials (Fig. 3b), the PXRD patterns were indexed to the mixture of CdS and COF without impurity phases. Notably, with the increase of COF shell content, the intensity of characteristic peaks at ~5.6° and ~9.7° gradually increased. In addition, the electronic properties of the samples were further investigated by the X-ray photoelectron spectroscopy (XPS) (Fig. S4). As shown in the Cd 3d spectra (Fig. 3c), the peaks at 411.5 and 404.8 eV were attributed to Cd $3d_{3/2}$ and Cd $3d_{5/2}$ for P-CdS, while the peaks of Cd $3d_{3/2}$ and Cd $3d_{5/2}$ for CdS@COF-*X* shifted to 411.9 and 405.2 eV, respectively [42,43]. Furthermore, Fig. 3d shows the S 2p spectrum of P-CdS, in which the main peaks are located at 162.3 and 161.2 eV belonging to S $2p_{1/2}$ and S $2p_{3/2}$, respectively [42,43]. Compared with P-CdS, the binding energies of S $2p_{1/2}$ and S $2p_{3/2}$ in CdS@COF-*X* both displayed a positive shift. Thus, the changes in the binding energies of Cd and S indicated a strong interaction between the CdS core and the COF shell for CdS@COF-*X* hybrid materials, excluding simple physical contact [42,43]. In addition, two fitted component peaks at 400.0 and 398.7 eV belonged to N–C and sp^2-hybridized N atoms in triazine units (C–N=C) for the N 1s XPS spectra (Fig. S5), respectively [40]. As for O 1s XPS spectra (Fig. S6), two peaks were attributable to C=O at 531.5 eV and the surface adsorbed oxygen species (O*) at 532.9 eV, respectively [41].

Uranium extraction experiment

The obtained samples were utilized as photocatalysts for sacrificial agents-free U(VI) photoreduction in an air atmosphere. Fig. 4a shows the U(VI) adsorption profiles of various samples

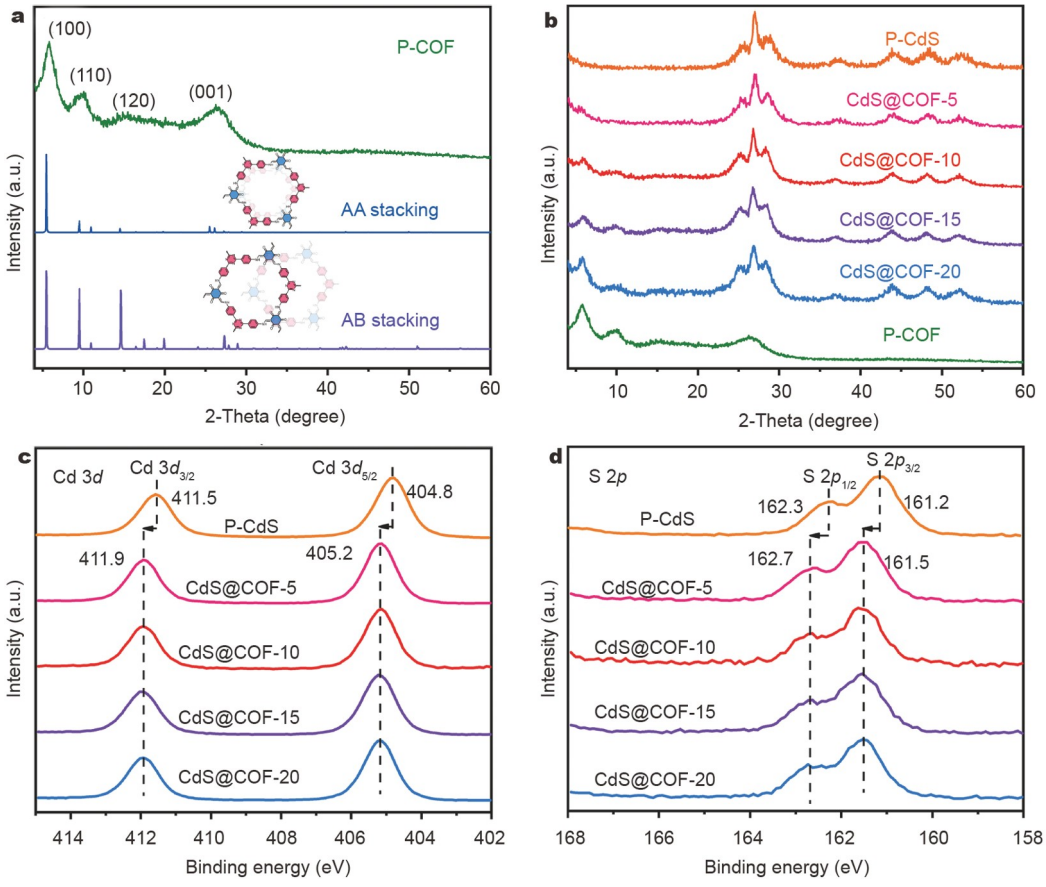

Figure 3 (a) PXRD patterns for experimental and different simulation of P-COF. (b) PXRD patterns of P-CdS, CdS@COF-*X*, and P-COF. (c) Cd 3d and (d) S 2p XPS spectra of P-CdS and CdS@COF-*X*.

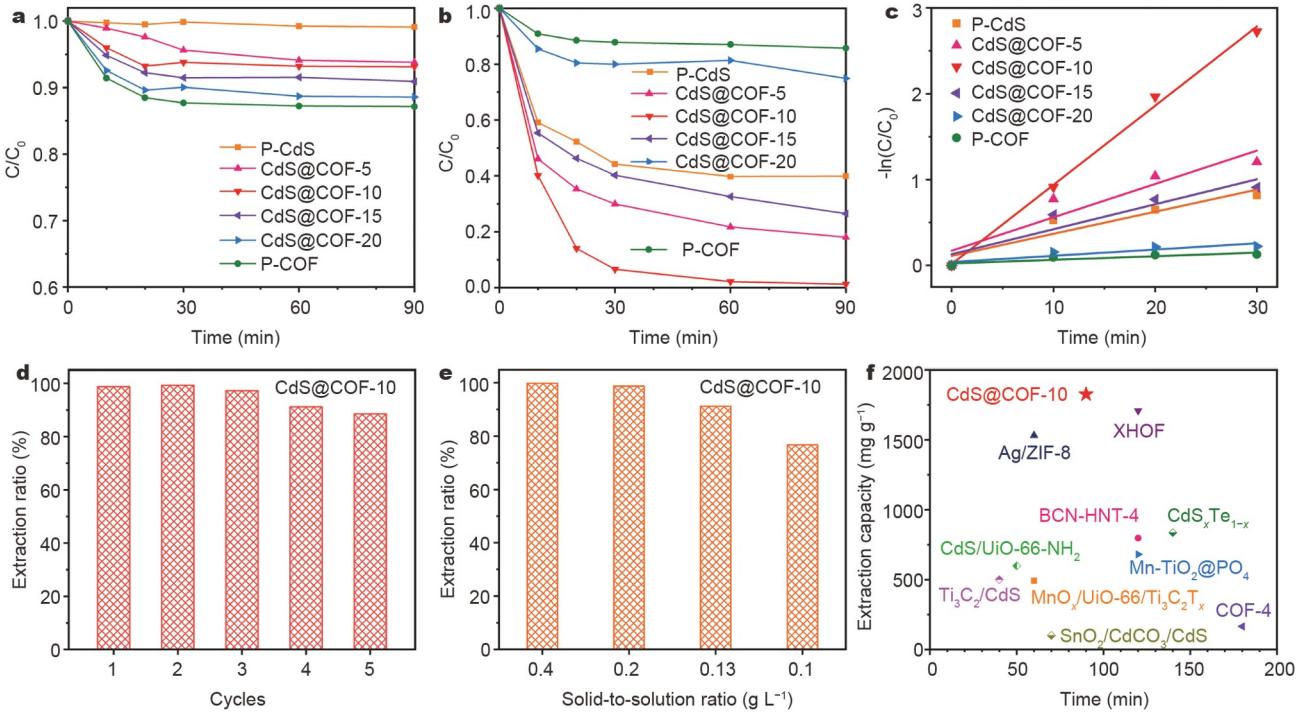

Figure 4 Concentration of U(VI) *versus* time *via* P-CdS, CdS@COF-*X*, and P-COF (a) under dark conditions and (b) under light conditions. (c) Reaction kinetics plots of U(VI) photoreduction *via* P-CdS, CdS@COF-*X*, and P-COF. U(VI) extraction ratios *via* CdS@COF-10 (d) over the course of five successive reaction rounds and (e) with different solid-to-solution ratios. (f) U(VI) extraction capacity *via* CdS@COF-10 and other reported catalysts towards U(VI) photoreduction without sacrificial agents.

over time under dark conditions. Without light irradiation, P-CdS demonstrated almost no adsorption effect on U(VI). With the increase in COF shell content, the adsorption capacity of CdS@COF-*X* on U(VI) increased gradually. When it came to P-COF, the U(VI) removal ratio and adsorption capacity were 12.9% and 153.5 mg g^{-1}, respectively. We further used the kinetic models to describe the adsorption behavior of P-COF. As shown in Fig. S7, the U(VI) adsorption over P-COF conformed to the pseudo-second-order kinetics (R^2 = 0.99842) rather than pseudo-first-order kinetics (R^2 = 0.67591), indicating the dominance of chemisorption. When a xenon lamp with the wavelength of full-spectrum and the intensity of 200 mW cm^{-2} was utilized to irradiate the reaction system, P-COF displayed practically identical U(VI) extraction behavior as in the absence of light (Fig. 4b). Interestingly, the extraction capacity and kinetics of U(VI) by P-CdS and CdS@COF-*X* were significantly enhanced under illumination. In particular, the extraction efficiency of U(VI) by CdS@COF-10 in a U(VI) solution with an initial concentration of 1 mmol L^{-1} reached 98.8% after 90 min. To further assess the reaction kinetics, the extraction rate constant (k) was calculated on different samples. Fig. 4c illustrates the fitting outcomes, where the order of k values is as follows: CdS-COF-10 (0.092 min^{-1}) > CdS-COF-5 (0.039 min^{-1}) > CdS-COF-15 (0.029 min^{-1}) > P-CdS (0.026 min^{-1}) > CdS-COF-20 (0.007 min^{-1}) > P-COF (0.004 min^{-1}). As such, CdS-COF-10 with appropriate COF shell content exhibited the highest U(VI) extraction capacity under illumination.

In order to investigate the photocorrosion resistance of CdS@COS-10, the concentration of cadmium (Cd) in solution during the photoreaction was measured. The Cd element was released gradually into the solution with the duration of irradiation for P-CdS, reaching a concentration of 69.8 mg L^{-1} after 90 min (Fig. S8). As for CdS@COF-10, the Cd concentration in solution was just 6.9 mg L^{-1} after 90 min, indicating the excellent antiphotocorrosion ability caused by the protection of the COF shell. Moreover, the repetitive U(VI) photoreduction cycles were further conducted *via* CdS@COF-10 to evaluate its stability and reusability. As shown in Fig. 4d, the U(VI) removal ratio *via* CdS@COF-10 remained as high as 88.5% even after five cycles, indicating the outstanding stability during U(VI) photoreduction.

In addition, the U(VI) photoreduction experiments over CdS@COF-10 under different solid-to-liquid ratio, pH and coexisting ion conditions were systematically executed. As shown in Fig. 4e, when the solid-to-liquid ratio was increased to 0.1 g L^{-1}, CdS@COF-10 still maintained the U(VI) removal ratio of 76.7% after 90 min, corresponding to the U(VI) extraction capacity of 1825.6 mg g^{-1}. The U(VI) extraction capacity *via* CdS@COF-10 towards sacrificial agents-free U(VI) photoreduction is also superior to most reported catalysts (Fig. 4f and Table S1). Furthermore, CdS@COF-10 displayed brilliant U(VI) extraction ratio at pH from 3 to 7 (Fig. S9). Moreover, CdS@COF-10 also possessed excellent U(VI) extraction ratio and selectivity when U(VI) coexisted with 11 cations of rare-earth metals, transition metals, and alkaline earth metals (Fig. S10).

Photocatalytic mechanistic studies

To elucidate the mechanism of U(VI) extraction under light, CdS@COF-10 after the reaction were collected (named as CdS@COF-10-U) and analyzed. As shown in Fig. 5a, the diffraction peaks of CdS and COF were maintained well in the PXRD pattern of CdS@COF-10-U, indicating its good stability in the process of U(VI) photoreduction. More importantly, the

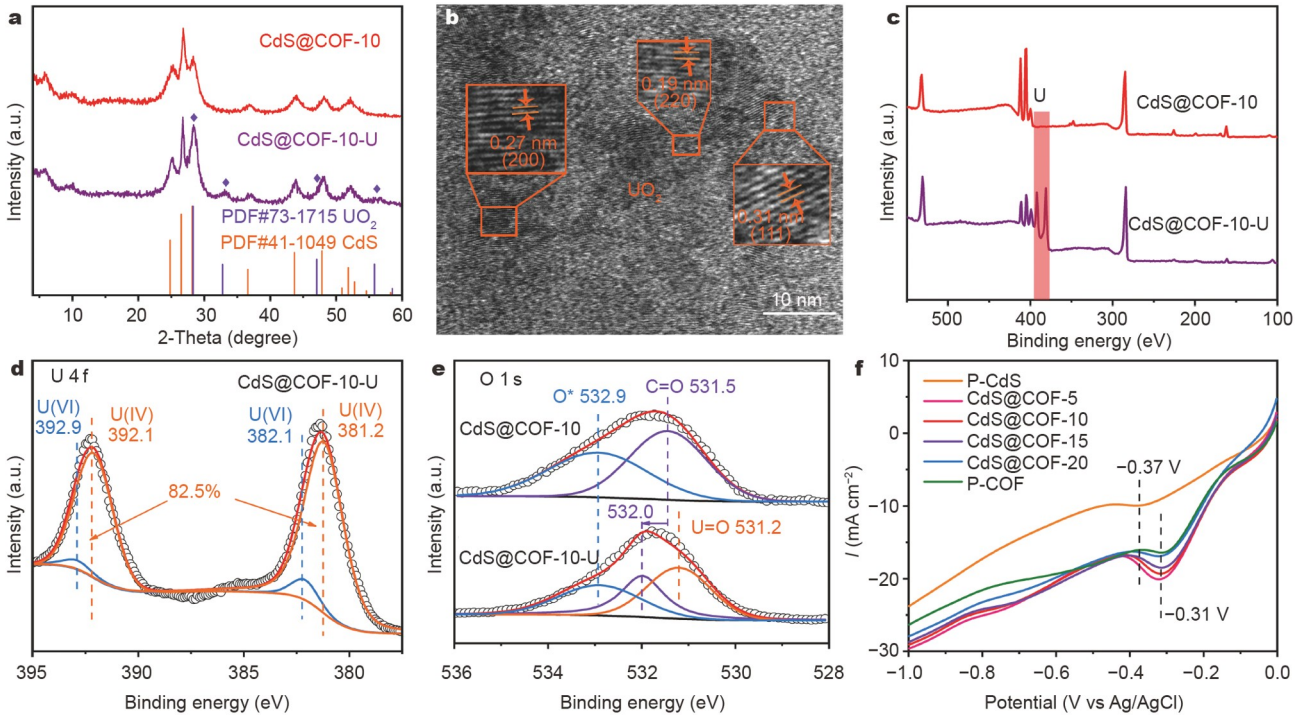

Figure 5 (a) PXRD patterns of CdS@COF-10 and CdS@COF-10-U. (b) TEM image of CdS@COF-10-U. (c) Full XPS spectra of CdS@COF-10 and CdS@COF-10-U. (d) U 4f XPS spectrum of CdS@COF-10-U. (e) O 1s XPS spectra of CdS@COF-10 and CdS@COF-10-U. (f) LSV curves of U(VI) reduction *via* P-CdS, CdS@COF-*X*, and P-COF.

PXRD pattern of CdS@COF-10-U displayed the characteristic signals of uranium dioxide (UO_2). Accordingly, the HAADF-STEM image and the associated EDX elemental mapping images displayed the distribution of uranium across the entire nanorod for CdS@COF-10-U (Fig. S11). Furthermore, the characteristic lattice spacing of UO_2 was also observed in the TEM image of CdS@COF-10-U (Fig. 5b), in which the lattice spacings of 3.1, 2.7, and 1.9 Å were corresponding to the (111), (200), and (220) crystal planes, respectively. In addition, the signal of uranium was found in the XPS spectrum of CdS@COF-10-U (Fig. 5c). In the U 4f XPS spectrum of CdS@COF-10-U (Fig. 5d), four constituent peaks were fitted, corresponding to U(VI) at 382.1 and 392.9 eV together with U(IV) at 381.2 and 392.1 eV, respectively [44–46]. The integral areas of U(IV) were much larger than these of U(VI), indicating that most of the extracted uranium was reduced *via* CdS@COF-10 during the reaction. Furthermore, the reduction ratio of uranium on CdS@COF-10-U was further calculated as 82.5%. As for the O 1s XPS spectrum of CdS@COF-10-U (Fig. 5e), the peak at 531.2 eV was ascribed to U=O [44]. More importantly, the binding energy of the C=O peak for CdS@COF-10-U was shifted from 531.5 to 532.0 eV compared with that for CdS@COF-10. Similarly, the positive shift of C–N binding energy for CdS@COF-10-U was also found in the N 1s XPS spectra (Fig. S12). Since the adsorption of U(VI) decreased the local electron density, C=O and the adjacent C–N were proved to be the main U(VI) chemisorption sites for CdS@COF-10 [47]. To highlight the importance of chemisorption of COF shell for CdS@COF-10 towards U(VI) photoreduction, we further measured the linear scanning voltammetry (LSV) curves in an electrolyte containing U(VI). As illustrated in Fig. 5f, P-CdS showed the weak U(VI) reduction peak at −0.37 V *versus* Ag/AgCl. The U(VI) reduction peaks of CdS@COF-*X* and P-COF were stronger and more positive compared with that of P-CdS, located at −0.31 V *versus* Ag/AgCl. This is attributed to the chemisorption of COF shell that can increase the effective collision between electrons and U(VI), and thus decreased the overpotential and activation energy of U(VI) reduction, which directly led to the outstanding catalytic activity towards U(VI) photoreduction for CdS@COF-10 [10].

To explain the significant activity of CdS@COF-10 in U(VI) photoreduction, the optical properties and band structures were further characterized. The enhancement in visible light absorption with increasing COF shell content was clearly observed in the ultraviolet-visible diffuse reflectance spectra of P-CdS and CdS@COF-*X* (Fig. S13). Furthermore, the band gaps of P-CdS and P-COF were calculated to be 2.56 and 2.43 eV by using Tauc plots, respectively (Fig. S14). In addition, based on the results of valence-band XPS spectra, the valence band (VB) positions of P-CdS and P-COF were determined to be 1.56 and 1.88 eV *versus* reversible hydrogen electrode (RHE), respectively (Fig. S15). Combining their band gap values, the conduction band (CB) positions of P-CdS and P-COF were obtained to be −1.00 and −0.55 eV *versus* RHE, respectively (Fig. S16).

To clarify the charge transfer direction and electronic coupling behavior of CdS core and COF shell after the coupling, we calculated their work functions and the charge redistribution between the heterojunction contact interfaces using density functional theory (DFT). As shown in Fig. 6a, b, the work functions of CdS and COF models were calculated to be 6.986 and 5.962 eV, respectively. In general, the electrons tend to cluster on the side of the material with larger work function after coupling, forming a typical built-in electric field [48,49]. In addition, the charge density differences are shown in Fig. 6c, where the blue and yellow regions represent the depletion and

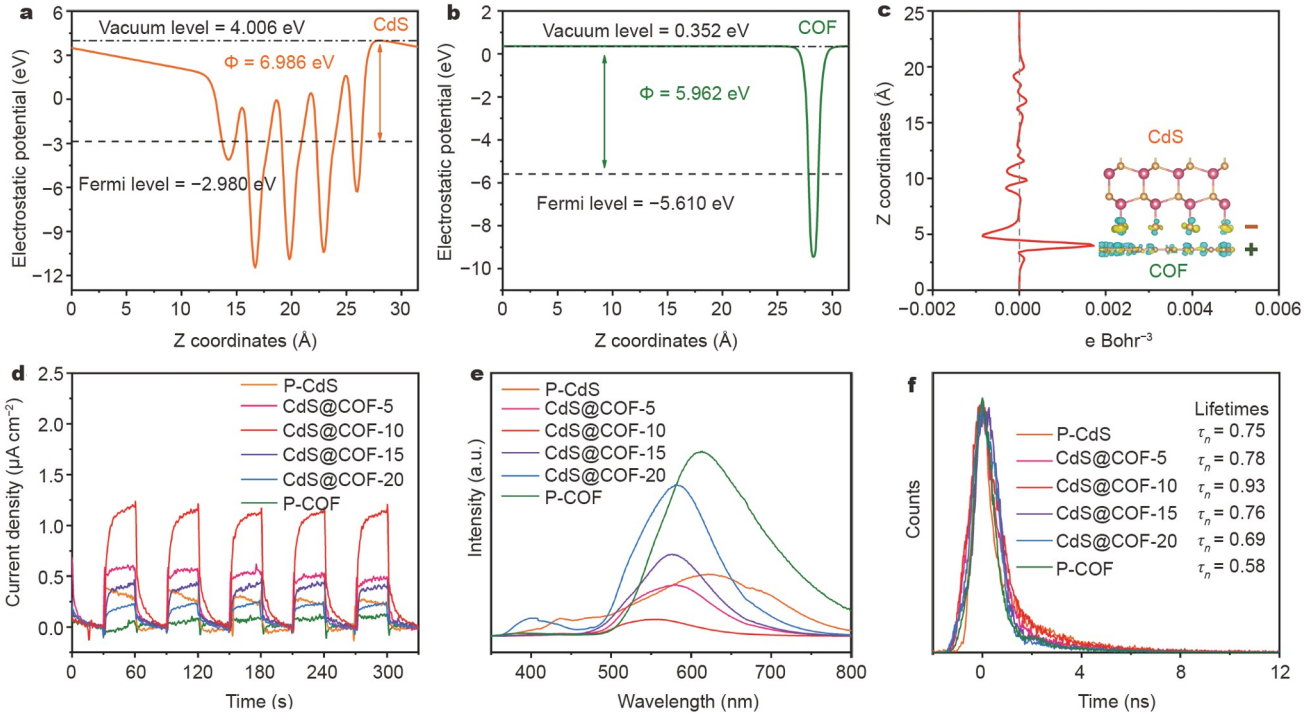

Figure 6 Calculated electrostatic potentials for (a) CdS and (b) COF models. (c) Profile of the plane-averaged differential charge density (*z*-axis) of the interface of CdS and COF models, with the simulated electron density distributions (illustration). (d) Transient photocurrent responses, (e) steady-state PL spectra, and (f) time-resolved PL spectra of P-CdS, CdS@COF-*X*, and P-COF.

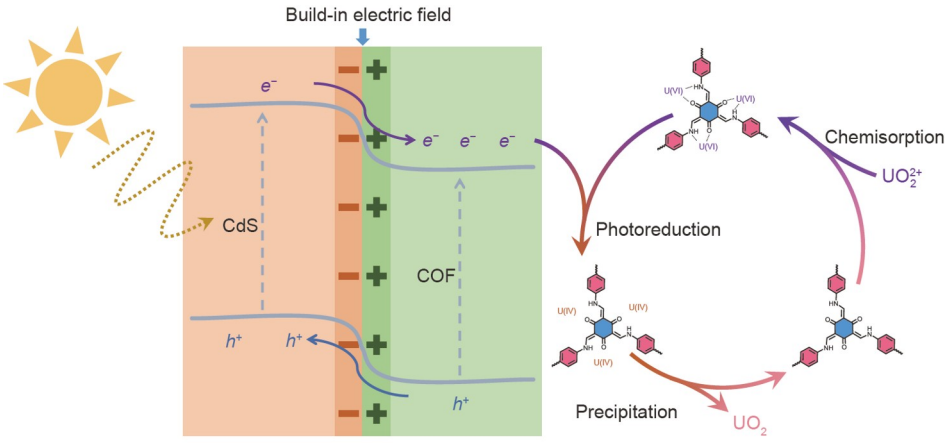

Figure 7 Schematic presentation of the reaction process over CdS@COF-10 towards U(VI) photoreduction.

accumulation of electrons, respectively. The heterojunction contact interface of CdS and COF models exhibited a significant surface charge redistribution phenomenon. The bader topology calculations revealed that each COF model transferred 0.607 e^- to the corresponding CdS model. Therefore, the electrons flowed from the COF shell into the CdS core after coupling, forming the built-in electric field at the interface for CdS@COF-*X*, which was favorable for carrier transfer at the interface.

In order to further explain the impact of the COF shell content on the photoreduction performance of CdS@COF-*X*, the transient photocurrent response of the synthesized samples was measured using photoelectrochemical methods. As shown in Fig. 6d, compared with P-CdS and P-COF, CdS@COF-*X* exhibited significant and stable photocurrents, with CdS@COF-10 showing the highest photocurrent intensity. The photocurrent intensity of the samples also corresponded to their performance towards U(VI) photoreduction. Moreover, we further analyzed the photoluminescence (PL) spectra of the samples to obtain the concrete evidences of transfer and recombination of photogenerated charge. Fig. 6e displays the steady-state PL spectra of obtained samples, in which P-COF and CdS@COF-10 show the highest and lowest intensities, respectively. As the COF shell content increases, the carrier separation efficiency of CdS@COF-*X* showed a pattern of increasing first and then decreasing. More importantly, we further studied the average emission decay time (τ_n) of photogenerated carriers by using time-resolved PL spectroscopy. As illustrated in Fig. 6f, the values of τ_n followed the order of CdS@COF-10 (0.93 ns) > CdS@COF-5 (0.78 ns) > CdS@COF-15 (0.76 ns) > P-CdS (0.75 ns) > CdS@COF-20 (0.69 ns) > P-COF (0.58 ns). Thus, for CdS-COF-5, the COF shell with low content was considered to have poor crystallinity and incomplete encapsulation, resulting in the generation of defects and incomplete interface contact, causing obstacles to carrier transfer [50]. As for CdS-COF-15 and CdS-COF-20, the COF shell with high content was believed to dominate light capture and hinder light absorption of the CdS core [51,52]. Therefore, CdS-COF-10 with appropriate COF shell content exhibited the highest photocurrent intensity, the most efficient carrier separation, and the longest carrier lifetime, contributing to the significant catalytic activity towards U(VI) photoreduction.

Based on the above results, the schematic diagram of the reaction mechanism for CdS-COF-10 towards U(VI) photoreduction was proposed (Fig. 7). First, the free U(VI) was bonded with C=O and the adjacent C–N on the COF shell by chemisorption. Under light, both the COF shell and the CdS core absorbed energy to produce photogenerated electrons and holes. Because of the strong built-in electric field at the interface, photogenerated electrons located in the CB of CdS were easily transferred to the CB of the COF shell and further effectively reduced the bound U(VI), leading to the precipitation of UO_2.

CONCLUSIONS

In conclusion, the CdS/COF core-shell nanorods (CdS@COF-10) with efficient chemisorption, enhanced carrier separation, and antiphotocorrosion ability were successfully constructed as highly active and stable catalyst for sacrificial agents-free U(VI) photoreduction. The COF shell not only provided chemisorption sites for U(VI) to decrease the activation energy of U(VI) reduction, but also formed a strong built-in electric field at the interface with the CdS core to promote the carrier separation. As such, the photogenerated electrons located in the CB of CdS were easily transferred to the CB of the COF shell and further effectively reduced the bound U(VI), leading to the precipitation of UO_2. Furthermore, for all CdS@COF-*X*, CdS-COF-10 with appropriate COF shell content balanced the crystallinity, interfacial contact integrity, light absorption of the CdS core, and number of U(VI) chemisorption sites, achieving the highest carrier separation efficiency and a record high U(VI) extraction capacity of 1825.6 mg L^{-1} after 90 min. This work not only provides a catalyst with excellent performance for sacrificial agents-free U(VI) photoreduction, but also expands the understanding of core-shell structure photocatalysts.

Received 28 June 2023; accepted 28 August 2023; published online 9 November 2023

1 Keener M, Hunt C, Carroll TG, *et al.* Redox-switchable carboranes for uranium capture and release. Nature, 2020, 577: 652–655
2 Huang Y, Yu Z, Zhang Q, *et al.* Constructing quinazolinone-anchored electron-rich covalent organic frameworks by photocatalytic reductive cyclization for idealizing iodine capture. Sci China Mater, 2023, 66: 2339–2345
3 Xie Y, Chen C, Ren X, *et al.* Emerging natural and tailored materials for uranium-contaminated water treatment and environmental remediation. Prog Mater Sci, 2019, 103: 180–234
4 Liu C, Hsu PC, Xie J, *et al.* A half-wave rectified alternating current electrochemical method for uranium extraction from seawater. Nat

Energy, 2017, 2: 17007
5 Feng L, Yuan Y, Yan B, *et al.* Halogen hydrogen-bonded organic framework (XHOF) constructed by singlet open-shell diradical for efficient photoreduction of U(VI). Nat Commun, 2022, 13: 1389
6 Gao Z, Wang Y, Lin Y, *et al.* Constructing dual-functional porphyrin-based thorium metal-organic framework toward photocatalytic uranium(VI) reduction integrated with organic oxidation. Sci China Chem, 2022, 65: 1544–1551
7 Chen T, Yu K, Dong C, *et al.* Advanced photocatalysts for uranium extraction: Elaborate design and future perspectives. Coord Chem Rev, 2022, 467: 214615
8 Li P, Wang J, Wang Y, *et al.* An overview and recent progress in the heterogeneous photocatalytic reduction of U(VI). J Photochem Photobiol C-Photochem Rev, 2019, 41: 100320
9 Zhang H, Liu W, Li A, *et al.* Three mechanisms in one material: Uranium capture by a polyoxometalate-organic framework through combined complexation, chemical reduction, and photocatalytic reduction. Angew Chem Int Ed, 2019, 58: 16110–16114
10 Yu K, Tang L, Cao X, *et al.* Semiconducting metal-organic frameworks decorated with spatially separated dual cocatalysts for efficient uranium (VI) photoreduction. Adv Funct Mater, 2022, 32: 2200315
11 Chen Z, Wang J, Hao M, *et al.* Tuning excited state electronic structure and charge transport in covalent organic frameworks for enhanced photocatalytic performance. Nat Commun, 2023, 14: 1106
12 Yu K, Li Y, Cao X, *et al. In-situ* constructing amidoxime groups on metal-free g-C_3N_4 to enhance chemisorption, light absorption, and carrier separation for efficient photo-assisted uranium(VI) extraction. J Hazard Mater, 2023, 460: 132356
13 Yuan Y, Niu B, Yu Q, *et al.* Photoinduced multiple effects to enhance uranium extraction from natural seawater by black phosphorus nanosheets. Angew Chem Int Ed, 2020, 59: 1220–1227
14 He P, Zhang L, Wu L, *et al.* Synergy of oxygen vacancies and thermoelectric effect enhances uranium(VI) photoreduction. Appl Catal B-Environ, 2023, 322: 122087
15 Chen T, Liu T, Zhou L, *et al.* Ternary boron carbon nitrides hollow nanotubes with tunable p-n homojunction for photo-assisted uranium extraction: A combined batch, EXAFS and DFT calculations. Appl Catal B-Environ, 2022, 318: 121815
16 Yu K, Shao P, Meng P, *et al.* Superhydrophilic and highly elastic monolithic sponge for efficient solar-driven radioactive wastewater treatment under one sun. J Hazard Mater, 2020, 392: 122350
17 Zhang Y, Zhu M, Zhang S, *et al.* Highly efficient removal of U(VI) by the photoreduction of SnO_2/$CdCO_3$/CdS nanocomposite under visible light irradiation. Appl Catal B-Environ, 2020, 279: 119390
18 Dong C, Qiao T, Huang Y, *et al.* Efficient photocatalytic extraction of uranium over ethylenediamine capped cadmium sulfide telluride nanobelts. ACS Appl Mater Interfaces, 2021, 13: 11968–11976
19 Liang P, Yuan L, Du K, *et al.* Photocatalytic reduction of uranium(VI) under visible light with 2D/1D Ti_3C_2/CdS. Chem Eng J, 2021, 420: 129831
20 Li Z, Zhang Z, Dong Z, *et al.* Solar light-responsive CdS/UiO-66-NH_2 for ultrafast uranium reduction from uranium-containing mine wastewater without external sacrificial agents. Separ Purif Tech, 2022, 283: 120195
21 Zhu Q, Xu Q, Du M, *et al.* Recent progress of metal sulfide photocatalysts for solar energy conversion. Adv Mater, 2022, 34: 2202929
22 Fu J, Yu J, Jiang C, *et al.* g-C_3N_4-based heterostructured photocatalysts. Adv Energy Mater, 2018, 8: 1701503
23 Das S, Pérez-Ramírez J, Gong J, *et al.* Core-shell structured catalysts for thermocatalytic, photocatalytic, and electrocatalytic conversion of CO_2. Chem Soc Rev, 2020, 49: 2937–3004
24 Liu M, Xing Z, Li Z, *et al.* Recent advances in core-shell metal organic frame-based photocatalysts for solar energy conversion. Coord Chem Rev, 2021, 446: 214123
25 Weng B, Qi MY, Han C, *et al.* Photocorrosion inhibition of semiconductor-based photocatalysts: Basic principle, current development, and future perspective. ACS Catal, 2019, 9: 4642–4687
26 Liu Y, Tan H, Wei Y, *et al.* Cu_2O/2D COFs core/shell nanocubes with antiphotocorrosion ability for efficient photocatalytic hydrogen evolution. ACS Nano, 2023, 17: 5994–6001
27 Huang N, Wang P, Jiang D. Covalent organic frameworks: A materials platform for structural and functional designs. Nat Rev Mater, 2016, 1: 16068
28 Geng K, He T, Liu R, *et al.* Covalent organic frameworks: Design, synthesis, and functions. Chem Rev, 2020, 120: 8814–8933
29 Liu R, Tan KT, Gong Y, *et al.* Covalent organic frameworks: An ideal platform for designing ordered materials and advanced applications. Chem Soc Rev, 2021, 50: 120–242
30 Wang GB, Xie KH, Xu HP, *et al.* Covalent organic frameworks and their composites as multifunctional photocatalysts for efficient visible-light induced organic transformations. Coord Chem Rev, 2022, 472: 214774
31 Yang Q, Luo M, Liu K, *et al.* Covalent organic frameworks for photocatalytic applications. Appl Catal B-Environ, 2020, 276: 119174
32 Li Y, Guo X, Li X, *et al.* Redox-active two-dimensional covalent organic frameworks (COFs) for selective reductive separation of valence-variable, redox-sensitive and long-lived radionuclides. Angew Chem Int Ed, 2020, 59: 4168–4175
33 Sun Q, Aguila B, Earl LD, *et al.* Covalent organic frameworks as a decorating platform for utilization and affinity enhancement of chelating sites for radionuclide sequestration. Adv Mater, 2018, 30: 1705479
34 Cui WR, Zhang CR, Jiang W, *et al.* Regenerable and stable sp^2 carbon-conjugated covalent organic frameworks for selective detection and extraction of uranium. Nat Commun, 2020, 11: 436
35 Leng R, Sun Y, Wang C, *et al.* Design and fabrication of hypercrosslinked covalent organic adsorbents for selective uranium extraction. Environ Sci Technol, 2023, 57: 9615–9626
36 Yang H, Hao M, Xie Y, *et al.* Tuning local charge distribution in multicomponent covalent organic frameworks for dramatically enhanced photocatalytic uranium extraction. Angew Chem Int Ed, 2023, 62: e202303129
37 Kandambeth S, Mallick A, Lukose B, *et al.* Construction of crystalline 2D covalent organic frameworks with remarkable chemical (acid/base) stability *via* a combined reversible and irreversible route. J Am Chem Soc, 2012, 134: 19524–19527
38 Zhong X, Ren Z, Ling Q, *et al.* Adsorption-photocatalysis processes: The performance and mechanism of a bifunctional covalent organic framework for removing uranium ions from water. Appl Surf Sci, 2022, 597: 153621
39 Zhong X, Ling Q, Kuang P, *et al.* The role of functional-group-tuning in adsorption-photoreduction of U(VI) onto β-ketoenamine covalent organic frameworks photosystem. Chem Eng J, 2023, 467: 143415
40 Zhong X, Ling Q, Ren Z, *et al.* Immobilization of U(VI) onto covalent organic frameworks with the different periodic structure by photocatalytic reduction. Appl Catal B-Environ, 2023, 326: 122398
41 Li Y, Wu Q, Guo X, *et al.* Laminated self-standing covalent organic framework membrane with uniformly distributed subnanopores for ionic and molecular sieving. Nat Commun, 2020, 11: 599
42 Wang D, Zeng H, Xiong X, *et al.* Highly efficient charge transfer in CdS-covalent organic framework nanocomposites for stable photocatalytic hydrogen evolution under visible light. Sci Bull, 2020, 65: 113–122
43 Wang D, Li X, Zheng LL, *et al.* Size-controlled synthesis of CdS nanoparticles confined on covalent triazine-based frameworks for durable photocatalytic hydrogen evolution under visible light. Nanoscale, 2018, 10: 19509–19516
44 Wang D, Song J, Wen J, *et al.* Significantly enhanced uranium extraction from seawater with mass produced fully amidoximated nanofiber adsorbent. Adv Energy Mater, 2018, 8: 1802607
45 Yu K, Jiang P, Wei J, *et al.* Enhanced uranium photoreduction on $Ti_3C_2T_x$ MXene by modulation of surface functional groups and deposition of plasmonic metal nanoparticles. J Hazard Mater, 2022, 426: 127823
46 Yu K, Jiang P, Yuan H, *et al.* Cu-based nanocrystals on ZnO for uranium photoreduction: Plasmon-assisted activity and entropy-driven stability. Appl Catal B-Environ, 2021, 288: 119978
47 Jiang P, Yu K, Yuan H, *et al.* Encapsulating Ag nanoparticles into ZIF-8

as an efficient strategy to boost uranium photoreduction without sacrificial agents. J Mater Chem A, 2021, 9: 9809–9814
48 Yang Y, Zhao S, Bi F, *et al.* Highly efficient photothermal catalysis of toluene over Co_3O_4/TiO_2 p-n heterojunction: The crucial roles of interface defects and band structure. Appl Catal B-Environ, 2022, 315: 121550
49 Li Y, Zhang J, Chen Q, *et al.* Emerging of heterostructure materials in energy storage: A review. Adv Mater, 2021, 33: 2100855
50 Wang Y, Hu Z, Wang W, *et al.* Design of well-defined shell-core covalent organic frameworks/metal sulfide as an efficient Z-scheme heterojunction for photocatalytic water splitting. Chem Sci, 2021, 12: 16065–16073
51 Pan YX, You Y, Xin S, *et al.* Photocatalytic CO_2 reduction by carbon-coated indium-oxide nanobelts. J Am Chem Soc, 2017, 139: 4123–4129
52 Wu C, Xing Z, Yang S, *et al.* Nanoreactors for photocatalysis. Coord Chem Rev, 2023, 477: 214939

Acknowledgements This work was supported by the National Natural Science Foundation of China (22125605, 21976125, 22206137 and U2067211) and Sichuan University Postdoctoral Interdisciplinary Innovation Fund (10822041A2127). The authors thank Dr. Yue Qi for the XRD measurements at the Comprehensive Training Platform of the Specialized Laboratory at the College of Chemistry, Sichuan University. The authors are also grateful to Shiyanjia Lab (www.shiyanjia.com) for the PL, TEM, NMR, and XPS analysis. The support from the Fundamental Research Funds for the Central Universities and the Comprehensive Training Platform Specialized Laboratory, College of Chemistry, Sichuan University, is gratefully acknowledged.

Author contributions Yu K, Li Y, and Ma L designed the studies and wrote the paper. Yu K, He N, Dong C, and Jiang B synthesized the catalysts and performed the catalytic tests with support from Li X. Yu K, Zou Y, and Pei X performed material characterizations. He P performed DFT calculations. All authors contributed to the general discussion.

Conflict of interest The authors declare that they have no conflict of interest.

Supplementary information Experimental details and supporting data are available in the online version of the paper.

Kaifu Yu received his BSc (2018) and MSc (2021) degrees from the School of National Defence & Nuclear Science and Technology, Southwest University of Science and Technology. He is currently a PhD student under the supervision of Prof. Lijian Ma at the College of Chemistry, Sichuan University. His present research interest focuses on the design of covalent organic frameworks and their application in uranium extraction.

Pan He received his MSc degree in 2023 from the School of National Defence & Nuclear Science and Technology, Southwest University of Science and Technology. He is currently pursuing his PhD degree under the supervision of Prof. Lijian Ma at the College of Chemistry, Sichuan University. His present research interest focuses on the design of semiconductor photocatalysts towards U(VI) reduction.

Lijian Ma is currently a professor at the College of Chemistry, Sichuan University. He received his PhD degree in functional molecular chemistry from Okayama University in 2010. His research interests include (1) the design, synthesis, and application of covalent organic frameworks, (2) the preparation and separation performance of membrane materials, and (3) the novel separation methods and materials in radiochemistry.

具有高效化学吸附、增强的载流子分离及抗光腐蚀能力的CdS/COF核壳结构纳米棒用于光催化还原铀

喻开富[1†], 何攀[1†], 何宁宁[1], 李小锋[1], 董昌雪[2], 蒋博[1], 邹莹迪[1], 裴响[1], 李阳[1*], 马利建[1*]

摘要 基于半导体光催化剂将可溶的六价铀(U(VI))还原为不可溶的四价铀(U(IV))是一种简便、环保、高效的铀提取方法. 实现该技术的关键是开发在无牺牲剂情况下对于光催化还原铀具有高活性和稳定性的催化剂. 本文报道了一种新型CdS/COF核壳结构光催化剂(CdS@COF-10), 该催化剂具有高效的化学吸附、增强的载流子分离和抗光腐蚀能力, 无需额外的牺牲剂即可用于高效的光催化还原铀. COF壳层不仅为U(VI)提供了化学吸附位点, 降低了U(VI)还原的活化能, 而且在与CdS核的界面处形成了内建电场, 促进了载流子的分离. 更重要的是, 具有适当COF壳含量的CdS-COF-10在结晶度、界面接触完整性、CdS核的光吸收和U(VI)化学吸附位点数量之间取得了平衡, 获得了最高的载流子分离效率和光催化还原铀性能.

